Original paper

H*T* breakdown of Mn-bearing elbaite from the Anjanabonoina pegmatite, Madagascar

Paolo BALLIRANO[1], Beatrice CELATA[1*], Henrik SKOGBY[2], Giovanni B. ANDREOZZI[1], Ferdinando BOSI[1]

[1] *Department of Earth Sciences, Sapienza University of Rome, Piazzale Aldo Moro 5, I-00185 Rome, Italy; beatrice.celata@uniroma1.it*

[2] *Department of Geosciences, Swedish Museum of Natural History, SE-10405 Stockholm, Sweden*

[*] *Corresponding author*

The thermal behavior of a gem-quality purplish-red Mn-bearing elbaite from the Anjanabonoina pegmatite, Madagascar, with composition $^{X}(Na_{0.41}\square_{0.35}Ca_{0.24})_{\Sigma1.00}{}^{Y}(Al_{1.81}Li_{1.00}Fe^{3+}{}_{0.04}Mn^{3+}{}_{0.02}Mn^{2+}{}_{0.12}Ti_{0.004})_{\Sigma3.00}{}^{Z}Al_6[^{T}(Si_{5.60}B_{0.40})_{\Sigma6.00}O_{18}](BO_3)_3(OH)_3{}^{W}[(OH)_{0.50}F_{0.13}O_{0.37}]_{\Sigma1.00}$ was investigated using both *in situ* High-Temperature X-Ray powder diffraction (H*T*-pXRD) and *ex situ* X-Ray single-crystal diffraction (SC-XRD) on two single crystals previously heated in the air up to 750 and 850 °C. The first occurrence of mullite diffraction peaks allowed us to constrain the breakdown temperature of Mn-bearing elbaite at ambient pressure, at 825 °C. The breakdown products from the H*T*-pXRD experiments were cooled down to ambient temperature and identified via pXRD, represented by B-mullite and γ-$LiAlSi_2O_6$. A thermally induced oxidation of Mn^{2+} to Mn^{3+} was observed with both *in-situ* and *ex-situ* techniques; it started at 470 °C and is assumed to be counterbalanced by deprotonation, according to the equation: $Mn^{2+} + (OH)^- \rightarrow Mn^{3+} + O^{2-} + 1/2H_2$. At temperatures higher than 752 °C, a partial disorder between the *Y* and *Z* sites is observed from unit-cell parameters and mean bond distances, possibly caused by the inter-site exchange mechanism $^{Y}Li + {}^{Z}Al \rightarrow {}^{Z}Li + {}^{Y}Al$.

Keywords: lithium tourmaline; high-temperature breakdown; powder X-Ray diffraction; crystal-structure refinement; single-crystal X-Ray diffraction

Received: 30 December 2021; accepted: 10 June 2022; handling editor: J. Cempírek

The online version of this article (doi: 10.3190/jgeosci.347) contains supplementary electronic material.

1. Introduction

Among borosilicates, minerals of the tourmaline supergroup show an extensive occurrence in various geological settings, from diagenetic stages to UHP environments, because of their flexible composition and structural stability (e.g., Dutrow and Henry 2011). In the tourmaline structure, cations are accommodated in a relatively large number of constituent-coordination environments (Bosi 2018), as it follows from the general chemical formula (Henry et al. 2011): $XY_3Z_6(T_6O_{18})(BO_3)_3V_3W$, where where $X = Na^+$, K^+, Ca^{2+}, □ (= vacancy); $Y = Al^{3+}$, Fe^{3+}, Cr^{3+}, V^{3+}, Mg^{2+}, Fe^{2+}, Mn^{2+}, Li^+; $Z = Al^{3+}$, Fe^{3+}, Cr^{3+}, V^{3+}, Mg^{2+}, Fe^{2+}; $T = Si^{4+}$, Al^{3+}, B^{3+}; B = B^{3+}; V = $(OH)^-$, O^{2-}; *W* = $(OH)^-$, F^-, O^{2-}. Note that the letters *X*, *Y*, *T*, *Z* and *B* represent groups of cations at the $^{[9]}X$, $^{[6]}Y$, $^{[6]}Z$, $^{[4]}T$ and $^{[3]}B$ crystallographic sites (designated by *italicized letters*). The letters V and W in the formula represent groups of anions accommodated at the [3]-coordinated O(3) and O(1) crystallographic sites, respectively.

Many attempts to define the *X–P–T* stability of tourmaline are known to date, the majority of which converge to breakdown temperatures confined between 700 and 920 °C, depending on composition, at pressures up to nearly 8 GPa (e.g., van Hinsberg et al. 2011). However, most data come from artificial systems, where tourmaline was added in excess to its ground host rock and the considered system was multiphase (e.g., Ota et al. 2008). At the same time, the high-temperature modifications of tourmaline alone were described in detail for Fe-dominant tourmalines and Fe–Mn-bearing elbaite (e.g., Fuchs et al. 1995, 2002; Pieczka and Kraczka 2004; Castañeda et al. 2006; Bačík et al. 2011; Bosi et al. 2019, and references therein). A common feature of the last experimental works is that they were principally focused on the Fe oxidation process. Besides, the thermal behavior of tourmaline needs to be fully described, and breakdown conditions, as well as post-breakdown products, need to be identified, similarly to what was recently reported for a Fe-rich fluor-elbaite in Celata et al. (2021).

The present work is focused on thermal behavior, breakdown temperature and products of a gem-quality natural sample of Mn-bearing elbaite from the Anjanabonoina pegmatite (Madagascar), with formula $^{X}(Na_{0.41}\square_{0.35}Ca_{0.24})_{\Sigma1.00}{}^{Y}(Al_{1.81}Fe^{3+}{}_{0.04}Li_{1.00}Mn^{3+}{}_{0.02}Mn^{2+}{}_{0.12}Ti_{0.01})_{\Sigma3.00}{}^{Z}Al_6{}^{T}(Si_{5.60}B_{0.40})_{\Sigma6.00}B_{3.00}O_{27}{}^{V}(OH)_3{}^{W}[(OH)_{0.50}F_{0.13}O_{0.37}]_{\Sigma1.00}$, structurally and chemically characterized by Bosi et al. (2021) at room conditions, and spectroscopi-

Tab. 1 Single-crystal X-ray diffraction data details for samples of tourmaline from Madagascar heated in the air up to 750 °C and 850 °C, respectively

Sample	dhth750b	dhth850a
crystal size (mm)	0.28 × 0.25 × 0.20	0.40 × 0.20 × 0.04
a (Å)	15.7819(2)	15.7809(2)
c (Å)	7.08590(10)	7.09390(10)
V (Å^3)	1528.42(4)	1529.96(4)
Data collection range, 2Θ(°)	6–75	6–75
hkl range	$-26 \le h \le 26$	$-23 \le h \le 26$
	$-23 \le k \le 26$	$-26 \le k \le 26$
	$-11 \le l \le 9$	$-12 \le l \le 11$
Number of reflections	11203	11409
Unique reflections, R_{int} (%)	1770, 0.98	1872, 1.26
Flack parameter	0.05(6)	0.05(6)
wR_2 (%)	3.23	3.35
R_1 (%) all data	1.2	1.30
R_1 (%) for $I > 2\sigma(I)$	1.2	1.27
GooF	1.120	1.097
Largest diff. peak and hole (±e$^-$/Å^3)	–0.33 and 0.29	–0.32 and 0.31

R_{int} – merging residual value; R_1 – discrepancy index, calculated from *F*-data; wR_2 – weighted discrepancy index, calculated from F^2 data; GooF – goodness of fit; Diff. Peaks – maximum and minimum residual electron density; Data collection temperature = 20 °C; Space-group *R*3*m*; *Z* = 3; MoK_α radiation (0.71073 Å); Redundancy = 12; Absorption correction method – SADABS; Structural refinement program – SHELXL-2013.

cally characterized before and after thermal treatment at 750 °C. In order to complete the study of Bosi et al. (2021) with structural data from a treated sample, *in situ* structure behavior, and information on elbaite breakdown products, we applied a dual approach using both *in situ* and *ex situ* experiments, respectively, High-Temperature powder X-Ray diffraction (H*T*-pXRD) and single-crystal X-Ray diffraction (SC-XRD).

2. Experimental

2.1. Thermal treatment at 750 and 850 °C

Two crystal fragments of the Mn-bearing elbaite were heated in air at 750 °C (labeled as dhth750b) and 850 °C (labeled as dhth850a). Next, the samples were placed in a gold container and pushed into a pre-heated horizontal-tube furnace equipped with a quartz-glass tube. The heating experiments lasted for 90 and 6 hours, respectively, and the runs were ended by pushing the samples out to the cold zone of the quartz tube, leading to cooling down to 100 °C within 1 minute.

2.2. SC-XRD and SREF

The two tourmaline fragments heated in air at 750 and 850 °C were analyzed by the single-crystal X-Ray Diffraction on a Bruker KAPPA APEX-II single-crystal diffractometer (Sapienza University of Rome, Earth Sciences Department), equipped with a charge-coupled device (CCD) area detector (6.2 × 6.2 cm active detection area, 512 × 512 pixels) and a graphite-crystal monochromator using MoK_α radiation from a fine-focus sealed X-ray tube. The sample-to-detector distance was 4 cm. A total of 3577 exposures (step = 0.2°, time/step = 20 s) covering a full-sphere with an average redundancy of ~12 was collected. Final unit-cell parameters were refined using the Bruker AXS SAINT program on reflections with $I > 10\ \sigma(I)$ in the range $6° < 2\theta < 75°$. The intensity data were processed and corrected for Lorentz, polarization and background effects using the APEX2 software program of Bruker AXS. The data were corrected for absorption using a multi-scan method (SADABS, Bruker AXS). The absorption correction led to an improvement in R_{int} (from ~0.024 to ~0.017 for both samples). No violation of *R*3*m* symmetry was detected. Single crystal Structure REFinement (SREF) was done using the SHELXL-2013 program (Sheldrick 2015). Starting coordinates were taken from Bosi et al. (2021). Variable parameters were scale factor, extinction coefficient, atom coordinates, site-scattering values (for *X*, *Y* and *Z* sites) and atomic-displacement factors. Attempts to refine the extinction coefficient yielded values within its standard uncertainty, thus, it was not refined. Neutral scattering factors were used for the cations and oxygen atoms. The atomic model refinement is similar to that used for the untreated Mn-bearing elbaite (see Bosi et al. 2021, for details).

All the single-crystal diffraction data are listed in Tabs 1, 2 and 3; CIF files are available as electronic supplementary material.

2.3. HT-pXRD

A crystal fragment of Mn-bearing elbaite was ground in an agate mortar under ethanol. The powder was loaded in a 0.7 mm diameter SiO_2-glass capillary that was kept open at one side. The capillary was fixed to a hollow corundum tube using Resbond® 989 and mounted and aligned on a standard goniometer head. A prototype of a heating chamber for capillaries, developed by MRI and Bruker AXS, was used for HT measurements. Details on the thermal calibration procedure of the chamber may

be found in Ballirano and Melis (2007).

In situ H*T*-pXRD data were collected on a Bruker AXS D8 Advance operating in θ/θ geometry in transmission mode. The investigated thermal range was 30–900 °C. The incident beam is focussed onto the capillary using a multilayer graded Göbel mirror. Soller slits are placed along with both the incident (2.3° opening angle) and diffracted (radial) beams. Data were measured with a position sensitive detector (PSD) VÅntec-1 set at an opening angle of 6° 2θ. Details of the data collection are listed in Tab. 4. Each diffraction pattern required 5.5 h of counting time and the whole high-T experiment took ca. 8 days.

After reaching the maximum temperature of 900 °C, the powder was cooled back to ambient temperature (R*T*) within the chamber (estimated cooling rate of ca. 10 °C min^{-1}). The capillary was opened at one side and the powder was removed, re-homogenized in an agate mortar and charged in a new borosilicate-glass capillary following the same procedure reported in Celata et al. (2021). It is worth mentioning that this procedure was adopted to avoid the probable occurrence of textured recrystallization at the walls of the capillary. However, re-homogenization included powder lying at the coldest extremity of the capillary where *T*, owing to thermal gradients, was considerably lower than that recorded by the thermocouple placed near the area bathed by the X-rays.

The diffraction data were evaluated by the Rietveld method using Topas V.6 (Bruker AXS 2016). The peak shape was modeled using the Fundamental Pa-

Tab. 2 Fractional atom coordinates, equivalent isotropic and isotropic displacement parameters (Å²) and site occupancies for the treated samples of tourmaline from Madagascar.

Sample/site	*x*	*y*	*z*	U_{eq}	Site occupancy
dhth750b					
X	0	0	0.2196(2)	0.0209(5)	$Na_{0.37}Ca_{0.29}$
Y	0.12172(3)	0.06086(2)	0.63800(9)	0.00761(14)	$Li_{0.25}Al_{0.69}Mn_{0.06}$
Z	0.29674(2)	0.26008(2)	0.60744(6)	0.00609(6)	$Al_{1.00}$
B	0.10913(5)	0.21826(9)	0.4516(2)	0.00597(19)	$B_{1.00}$
T	0.19144(2)	0.18960(2)	0	0.00496(7)	$Si_{0.92}B_{0.08}$
O1	0	0	0.7730(3)	0.0193(4)	$O_{0.87}F_{0.13}$
O2	0.05999(4)	0.11999(7)	0.48839(17)	0.01290(19)	$O_{1.00}$
O3	0.26096(9)	0.13048(4)	0.50727(15)	0.01177(17)	$O_{1.00}$
O4	0.09388(4)	0.18775(8)	0.07465(16)	0.01060(16)	$O_{1.00}$
O5	0.18572(8)	0.09286(4)	0.09511(15)	0.01096(16)	$O_{1.00}$
O6	0.19395(5)	0.18384(5)	0.77404(11)	0.00745(11)	$O_{1.00}$
O7	0.28650(5)	0.28590(4)	0.07599(10)	0.00719(11)	$O_{1.00}$
O8	0.20942(5)	0.27002(5)	0.43693(11)	0.00728(11)	$O_{1.00}$
H1	0	0	0.908(4)	0.023	$H_{0.38}$
H3	0.2538(18)	0.1269(9)	0.378(3)	0.014	$H_{1.00}$
dhth850a					
X	0	0	0.2185(2)	0.0209(5)	$Na_{0.36}Ca_{0.29}$
Y	0.12195(4)	0.06098(2)	0.63766(8)	0.00739(14)	$Li_{0.21}Al_{0.74}Mn_{0.06}$
Z	0.29663(2)	0.25981(2)	0.60671(6)	0.00621(7)	$Al_{1.00}$
B	0.10920(5)	0.21840(11)	0.4512(2)	0.0061(2)	$B_{1.00}$
T	0.19142(2)	0.18965(2)	0	0.00499(7)	$Si_{0.93}B_{0.08}$
O1	0	0	0.7706(3)	0.0178(4)	$O_{0.87}F_{0.13}$
O2	0.06005(4)	0.12009(8)	0.48791(17)	0.0121(2)	$O_{1.00}$
O3	0.26004(9)	0.13002(5)	0.50800(15)	0.01166(19)	$O_{1.00}$
O4	0.09403(4)	0.18806(9)	0.07532(16)	0.01086(18)	$O_{1.00}$
O5	0.18545(9)	0.09272(5)	0.09467(15)	0.01119(18)	$O_{1.00}$
O6	0.19346(5)	0.18369(5)	0.77381(11)	0.00756(12)	$O_{1.00}$
O7	0.28667(5)	0.28598(5)	0.07558(10)	0.00727(12)	$O_{1.00}$
O8	0.20948(5)	0.27008(5)	0.43647(11)	0.00739(12)	$O_{1.00}$
H1	0	0	0.906(4)	0.021	$H_{0.38}$
H3	0.2506(19)	0.1253(9)	0.380(3)	0.014	$H_{1.00}$

Tab. 3 Selected bond lengths (Å) for the treated tourmaline samples.

Sample	dhth750b	dhth850a	Sample	dhth750b	dhth850a
X–O2 (×3)	2.5135(16)	2.5194(16)	*Z* – m. a. n.	13	13
X–O5 (×3)	2.6872(12)	2.6823(13)	*B*–O2	1.3682(16)	1.3686(18)
X–O4 (×3)	2.7640(12)	2.7635(13)	*B*–O8 (×2)	1.3750(9)	1.3747(10)
<*X*–O>	2.655	2.655	<*B*–O>	1.372	1.372
X – m. a. n.	9.788(10)	9.842(11)	*B* – m. a. n.	5	5
Y–O1	1.9190(12)	1.9150(12)	*T*–O6	1.6053(8)	1.6086(8)
Y–O2 (×2)	1.9629(8)	1.9659(8)	*T*–O7	1.6032(6)	1.6039(7)
Y–O6 (×2)	1.9450(8)	1.9420(8)	*T*–O4	1.6145(4)	1.6155(5)
Y–O3	2.1166(13)	2.0995(13)	*T*–O5	1.6296(5)	1.6295(5)
<*Y*–O>	1.986	1.981	<*T*–O>	1.613	1.614
Y – m. a. n.	11.230(4)	11.670(4)	*T* – m. a. n.	13.307(3)	13.325(3)
Z–O6	1.8765(7)	1.8823(8)			
Z–O7	1.8820(7)	1.8832(7)			
Z–O8	1.8821(7)	1.8831(7)			
Z–O8'	1.8972(7)	1.8973(8)			
Z–O7'	1.9380(7)	1.9409(7)			
Z–O3	1.9625(5)	1.9585(6)			
<*Z*–O>	1.906	1.908			

Tab. 4 Miscellaneous data of the data collection and Rietveld refinements. Definition of the statistical indicators as indicated in Young (1993).

2θ range (°)	7–145
2θ step-size (°)	0.021798
Counting time (s)	3
T_{max} (°C)	900
T steps (°C)	25
$*R_p$ (%)	1.889–2.198
$*R_{wp}$ (%)	2.375–2.772
$*R_{Bragg}$ (%)	0.732–1.162
$*D_{Wd}$	0.796–1.130
χ^2	1.396–1.590

* – Up to 825 °C, i.e., before starting the breakdown process.

rameters Approach (Cheary and Coelho 1992). An absorption correction was applied using the equation of Sabine et al. (1998) for a cylindrical sample and the procedure described by Ballirano and Maras (2006) was followed for handling the correlation existing between displacement parameters and absorption. The isotropic displacement parameters were constrained as follow: $B_Y = B_Z = B_B = B_T$; $B_{O2} = B_{O3} = B_{O4} = B_{O5} = B_{O6} = B_{O7} = B_{O8}$. The total site scattering at *Y*+*Z* sites was forced to be constant throughout the analyzed thermal range. Preferred orientation effects were corrected using spherical harmonics (8th-order, nine refinable parameters) following the procedure reported by Ballirano (2003) for selecting the appropriate number of terms. Starting structural data were those obtained from SREF (see below) and each refined structure at a given non-ambient *T* was used as input for the subsequent *T*.

3. Results and discussion

3.1. SC-XRD and SREF

Compared to the untreated sample of Bosi et al. (2021), the sample heated up to 750 °C (dhth750b) shows a reduction of the unit-cell *a*-parameter from 15.7935(4) to 15.7819(2) Å. In contrast, the *c*-parameter remains constant concerning the untreated sample (about 7.086 Å). The observed decrease in *a* can be interpreted as the result of the Mn oxidation from +2 to +3, which occurs approximately between 470 and 650 °C (Fig. 1). The oxidation of Mn is also supported by optical absorption data, which show a significant increase in the intensity of the Mn^{3+}-absorption band associated with the purplish-red color intensity of the treated sample reported in Bosi et al. (2021). Accordingly, a reduction in <*Y*–O> is observed, from 1.979 Å in the untreated sample to 1.975 Å in the heated one. The <*Z*–O> remains practically constant (1.906 Å), basically because the *Z* site is fully occupied by Al and therefore is not involved in the process. Therefore, the structural data for the sample dhth750b thermally treated at 750 °C confirm the ordered formula proposed by Bosi et al. (2021): $^{X}(Na_{0.41}\square_{0.35}Ca_{0.24})_{\Sigma1.00}\ ^{Y}(Al_{1.81}Li_{1.00}Fe^{3+}_{0.04}Mn^{3+}_{0.15}Ti_{0.004})_{\Sigma3.00}\ ^{Z}Al_6\ [^{T}(Si_{5.60}B_{0.40})_{\Sigma6.00}O_{18}]\ (BO_3)_3\ (OH)_3\ ^{W}[(OH)_{0.38}F_{0.13}O_{0.49}]_{\Sigma1.00.}$

In this regard, the observed increase of the Mn^{3+} absorption bands strongly support the Mn oxidation.

The sample heated up to 850 °C (dhth850a) shows an additional decrease of the *a*-parameter down to 15.7809(2) Å, together with a shortening of <*Y*–O> to 1.972 Å. As the oxidation process was ended, such behavior could be ascribed to the partial disorder generated by Al–Li substitution, with Li moving to the *Z* site and being substituted by Al (a smaller cation compared to Li) from the *Z* site, thus leading the YO_6 polyhedron to shrink. Alongside, Li slightly bulked the ZO_6 polyhedron up, leading to a <*Z*–O> of 1.908 Å from the previous value of 1.906 Å and sizing up the *c*-parameter to 7.0939(1) Å. The partial Li–Al disorder over *Y* and *Z* is also consistent with the refined *Y*-site scattering (in terms of mean atomic number, m. a. n.). *Y*-m. a. n. of sample dhth850a is significantly larger than those of samples dhth750b and untreated: respectively, 11.68(5) > 11.23(5) and 11.13(4), which reflects the presence of cations heavier than Li at the *Y* site (as, for example, Al), corresponding to the possible site populations $^{Y}(Al_{1.91}Li_{0.90}Fe^{3+}_{0.04}Mn^{3+}_{0.15}Ti_{0.004})_{\Sigma3.00}\ ^{Z}(Al_{5.90}Li_{0.10})_{\Sigma6.00.}$

3.2. HT-pXRD

3.2.1. Breakdown products

Miscellaneous information regarding the refinements is listed in Tab. 4, a magnified view of the whole data set, in the form of a pseudo-Guinier plot, is shown in Fig. 1 and a representative example of Rietveld plots

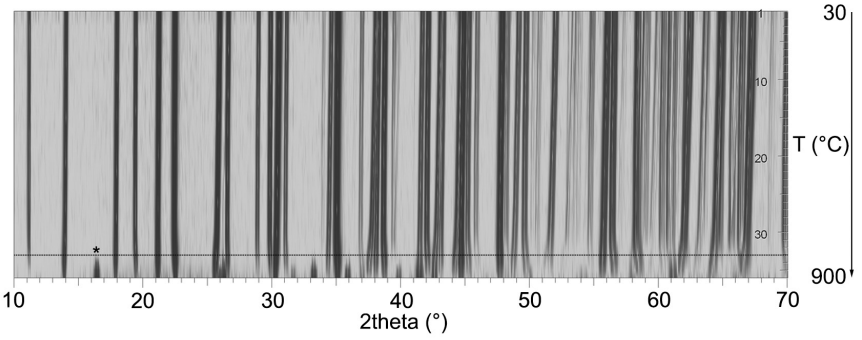

Fig. 1 Magnified view (10–70° 2θ) of the full data set of the heating cycle shown as a pseudo-Guinier plot.

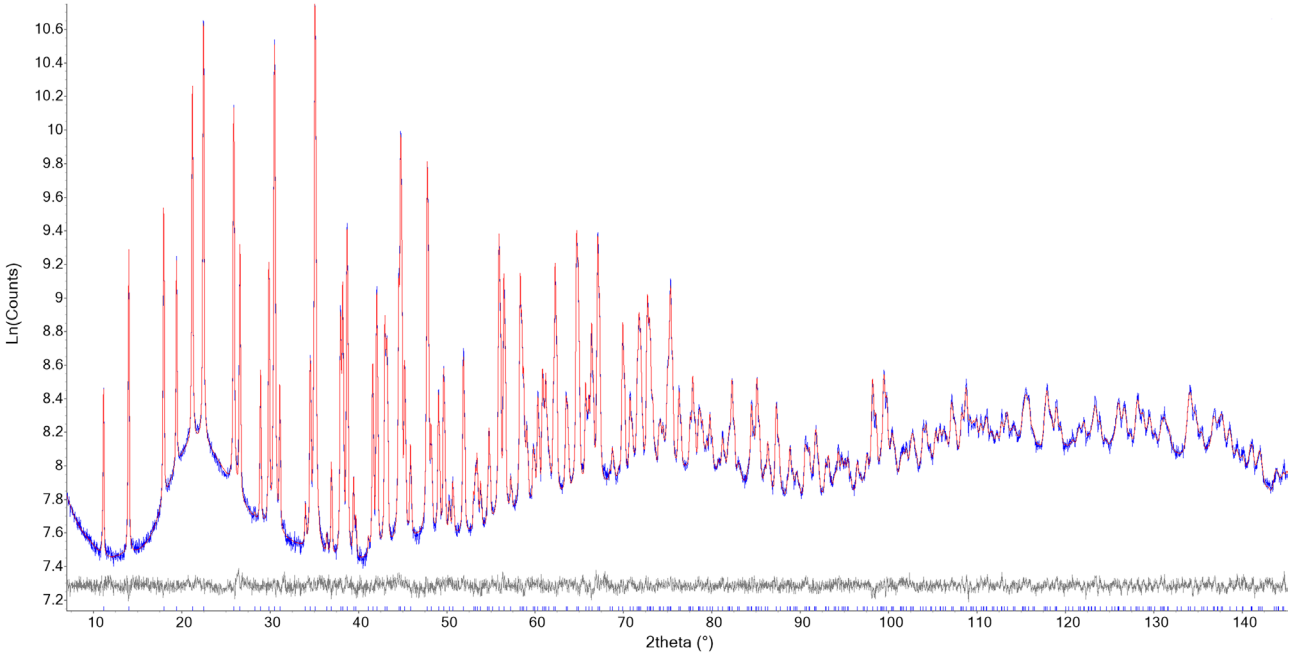

Fig. 2 Representative example of the Rietveld plots of the diffraction pattern collected at 275 °C. Blue: experimental; red: calculated; grey: difference; vertical bars: position of calculated Bragg reflections of the tourmaline studied. Intensities on a logarithmic scale.

in Fig. 2. CIF files of the structures refined at the various *T* are given in ESM.

The first evidence of the structural breakdown of the Mn-bearing elbaite was detected at 850 °C because of the occurrence of very weak diffraction reflections attributed to a mullite-like phase (marked with a star in Fig. 1). This is approximately the same temperature as reported for fluor-elbaite under similar experimental conditions (Celata et al. 2021). At higher *T*, the material consists prevalently of the mullite-like phase, and the diffraction patterns show a drastic reduction of tourmaline reflections intensities, preventing an accurate derivation of its structural parameters. Therefore, only cell parameters derived at 850 and 875 °C will be further discussed in

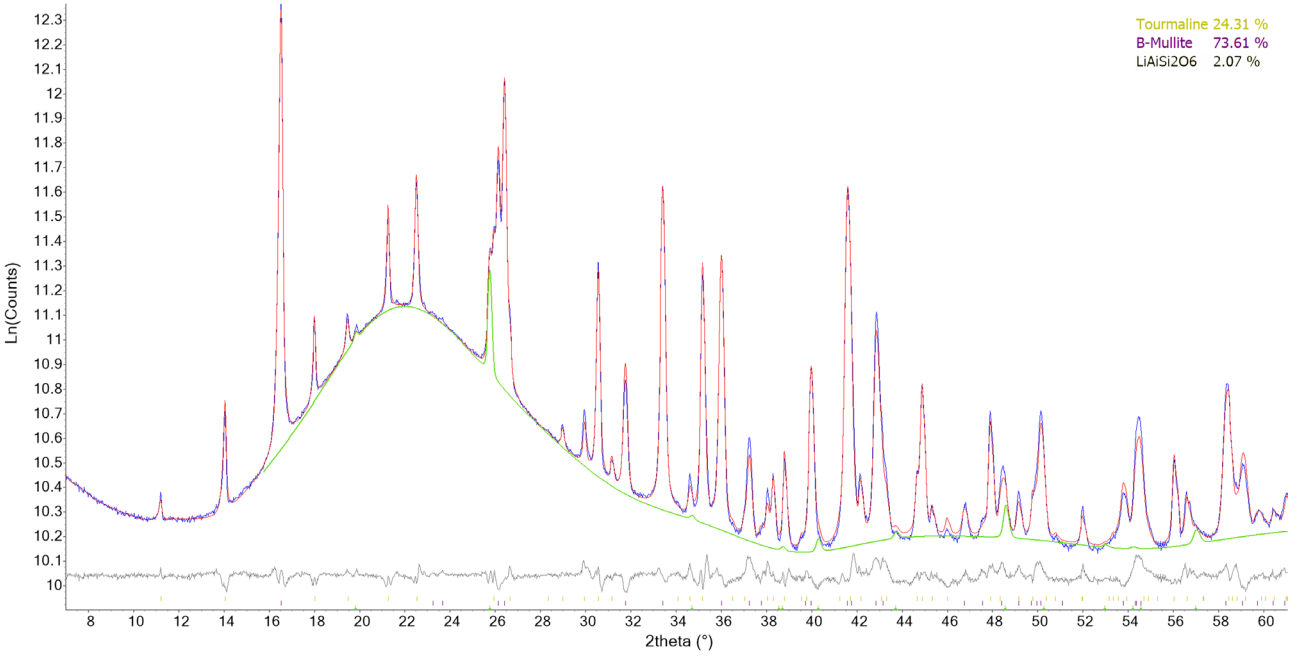

Fig. 3 Magnified 10–60° 2θ view of the Rietveld plots of the products of the breakdown of the tourmaline studied. Blue: experimental; red: calculated; green: calculated contribution of γ-$LiAlSi_2O_6$; grey: difference; vertical bars: position of calculated Bragg reflections of (from above to below) tourmaline (unreacted), B-mullite, and γ-$LiAlSi_2O_6$. Intensities on a logarithmic scale.

Tab. 5 Comparison of the unit-cell parameters of the tourmaline sample before and after thermal treatment.

	SCXRD		PXRD	
	Untreated	Treated	Untreated	Back ambient *T*
a (Å)	15.7935(4)	15.7819(2)	15.7928(1)	15.7752(3)
c (Å)	7.0860(2)	7.0859(1)	7.0842(1)	7.0917(2)
V (Å^3)	1530.69(9)	1528.42(4)	1530.16(2)	1528.38(7)

the following without any reference to possible structural modification. The breakdown was completed at 900 °C. Analysis of the diffraction pattern of the sample cooled down to ambient temperature (Fig. 3) clearly shows the prevailing mullite-like phase, occurrence of subordinate relicts of unreacted tourmaline caused by the re-homogenization of the powder (Celata et al. 2021), and presence of some amorphous material, likely a cooling product of a silicate melt derived from the tourmaline breakdown.

With respect to the Fe-rich fluor-elbaite (Celata et al. 2021) and Fe-dominant tourmalines heated in the air (e.g., Bačík et al. 2011), neither hematite nor spinel was detected here, along with B-mullite as breakdown products of tourmaline. Anyway, of particular interest is the occurrence of an additional relatively strong reflection at ca. 2θ = 25.75° (d = 3.457 Å). This reflection was not observed in the diffraction pattern of breakdown products of fluor-elbaite (Celata et al. 2021), and it can be assigned to the γ-polymorph of $LiAlSi_2O_6$ (space group $P6_222$; Li 1968). Naturally occurring as virgilite (French et al. 1978), this phase represents a stuffed β-quartz structure. It is worth noting the existence of a solid-solution series between β-quartz (QZ) and γ-$LiAlSi_2O_6$ (SP) and the observed material is expected to lay somewhere between the two end members. Reported unit-cell parameters for virgilite ($SP_{61}QZ_{39}$) are *a* = 5.132(1) Å, *c* = 5.454(1) Å (French et al. 1978) whereas those of synthetic γ-$LiAlSi_2O_6$ are *a* = 5.217(1) Å, *c* = 5.464(1) Å (Li 1968). For comparison, the refined cell parameters of the present breakdown product were *a* = 5.166(1) Å, *c* = 5.440(2) Å, pointing out a composition significantly displaced toward the SP endmember.

Unit-cell parameters of the mullite-like phase, refined in the space group *Pbam*, were *a* = 7.5151(2) Å, *b* = 7.6431(2) Å, *c* = 2.8157(1) Å, *V* = 161.73(1) Å^3 and are consistent with those of B-mullites (Lührs et al. 2014). Several anhydrous ternary B_2O_3–Al_2O_3–SiO_2 (BAS) phases are known (see for example Werding and Schreyer 1992; Buick et al. 2008; Grew et al. 2008; Novák et al. 2015; Cempírek et al. 2016) whose unit-cell volumes are multiple

Tab. 6 Refined unit-cell parameters and volume at the various *T*.

T (°C)	*a* (Å)	*c* (Å)	*V* (Å^3)	wt. % mullite-like	wt. % γ-$LiAlSi_2O_6$
30	15.7928(1)	7.0842(1)	1530.16(2)	–	–
50	15.7933(1)	7.0852(1)	1530.47(2)	–	–
75	15.7960(1)	7.0872(1)	1531.43(2)	–	–
100	15.7973(1)	7.0888(1)	1532.04(2)	–	–
125	15.7983(1)	7.0902(1)	1532.52(2)	–	–
150	15.8002(1)	7.0919(1)	1533.27(2)	–	–
175	15.8020(1)	7.0937(1)	1534.01(2)	–	–
200	15.8039(1)	7.0957(1)	1534.80(2)	–	–
225	15.8055(1)	7.0974(1)	1535.49(2)	–	–
250	15.8075(1)	7.0993(1)	1536.29(2)	–	–
275	15.8095(1)	7.1013(1)	1537.11(2)	–	–
300	15.8115(1)	7.1031(1)	1537.90(2)	–	–
325	15.8143(1)	7.1055(1)	1538.95(2)	–	–
350	15.8170(1)	7.1078(1)	1539.98(2)	–	–
375	15.8191(1)	7.1100(1)	1540.86(2)	–	–
400	15.8219(1)	7.1124(1)	1541.94(2)	–	–
425	15.8232(1)	7.1143(1)	1542.60(2)	–	–
450	15.8253(1)	7.1166(1)	1543.49(2)	–	–
475	15.8271(1)	7.1187(1)	1544.31(2)	–	–
500	15.8277(1)	7.1207(1)	1544.87(2)	–	–
525	15.8295(1)	7.1231(1)	1545.73(2)	–	–
550	15.8301(1)	7.1253(1)	1546.32(2)	–	–
575	15.8307(1)	7.1275(1)	1546.92(2)	–	–
600	15.8306(1)	7.1299(1)	1547.42(2)	–	–
625	15.8309(1)	7.1322(1)	1547.98(2)	–	–
650	15.8320(1)	7.1350(1)	1548.80(2)	–	–
675	15.8329(1)	7.1374(1)	1549.49(2)	–	–
700	15.8342(1)	7.1402(1)	1550.36(2)	–	–
725	15.8353(1)	7.1434(1)	1551.28(2)	–	–
750	15.8363(1)	7.1475(1)	1552.35(2)	–	–
775	15.8341(1)	7.1532(1)	1553.17(3)	–	–
800	15.8217(2)	7.1624(1)	1552.73(4)	–	–
825	15.8039(2)	7.1751(1)	1551.98(4)	–	–
850*	15.7896(2)	7.1880(1)	1551.95(4)	5.7(5)	–
875*	15.7790(3)	7.1971(2)	1551.85(6)	36.0(4)	tr.
900	–	–	–	96.4(2)	3.6(2)

tr. stands for "traces".

integers of the mullite one (ca. 168 Å^3) and an increased B content produces a progressive contraction. Unit cell parameters of the present B-mullite are smaller than those of the phase arising from the breakdown of fluor-elbaite (V = 164.22 Å^3; Celata et al. 2021), suggesting a higher content of B_2O_3. An estimation of the B content done using the regression equations proposed by Lührs et al. (2014) indicates ca. 16–17 mol. % B_2O_3.

A comparison between the chemical composition of the present and the fluor-elbaite sample (Celata et al. 2021) outlines a few relevant characteristics valuable to justify the correspondingly different breakdown products. Despite the higher B content of the present sample [0.40 atoms per formula unit (*apfu*) B are also allocated at T site], the Al/B ratio is almost equal (2.32 vs. 2.30 respectively). Differently, the Si/B ratio is lower in the present sample (1.65 *vs.* 2). Moreover, Li is more abundant in the present sample than in fluor-elbaite (1 *apfu vs.* 0.86 *apfu*). Finally, Fe (and to a minor extent Mn, and Zn) is present as traces in the present sample, whereas it exceeds 1 *apfu* in fluor-elbaite. The higher B content of the present pristine sample positively correlates with the estimated higher mol. % B_2O_3 of the B-mullite arising from its structural breakdown than that of the B-mullite produced from the fluor-elbaite breakdown. The occurrence of a Li-bearing crystalline material among the breakdown products of the present sample is reasonable due to its higher Li content compared to fluor-elbaite, where it was preferentially allocated into the glass phase. However, it is worth mentioning that high contents of Li have also been found in boromullite and vránaite (Novák et al. 2015; Cempírek et al. 2016), and, in principle, some Li could enter the structure of both B-mullite samples produced from tourmalines breakdown. The presence of different amounts of Li may potentially contribute to the observed differences in cell volume. The relevant transition elements content of fluor-elbaite is allocated, at the breakdown, in spinel and hematite. Such oxides are not observed in the breakdown products of the present sample owing to the minor content of Fe and Mn in the pristine material. Despite the Si/B ratio of the present recrystallized B-mullite being lower than that of pristine tourmaline (ca. 0.75–1 : 1 for an approximate $Al_{8.5}B_{1.5}Si_2O_{19}$–$Al_8B_2Si_2O_{19}$ composition as compared to 1.65 : 1), we may hypothesize that the Si-rich amorphous component retrieved at the end of the breakdown process still contains significant B. Moreover, considering the chemical composition of the pristine material, we may infer that the silicate amorphous component should also contain Na, Ca, Mn, Fe and H_2O.

Tab. 7 Refined unit-cell parameters and volume of the mullite-like phase at the various T.

T (°C)	a (Å)	b (Å)	c (Å)	V (Å^3)
850	7.555(1)	7.688(4)	2.8225(9)	163.9(1)
875	7.5504(3)	7.6911(3)	2.8244(1)	164.02(1)
900	7.5479(2)	7.6891(2)	2.8255(1)	163.98(1)

Interestingly, the unit-cell parameters of the relict tourmaline are reasonably close to those observed at ambient T for the sample heated at 850 °C and analyzed by SREF (Tab. 5). This suggests that this is the highest temperature in the coldest region of the capillary, located at ca. 4 cm from the center of the focussed X-ray beam, which has a width of ca. 12 mm.

3.2.2. Thermal expansion and HT structure modifications

The unit-cell parameters of the Mn-bearing elbaite at variable T are listed in Tab. 6, and the relative expansion of the same parameters for each T is shown in Fig. 4. Table 6 also reports the quantitative phase analysis (QPA) of the material in the 850–900 °C thermal range indicates a fast increase in the mullite-like phase content. Finally, Tab. 7 lists the unit-cell parameters of the mullite-like phase in the same 850–900 °C thermal range showing only marginal variations, as expected for refractory material.

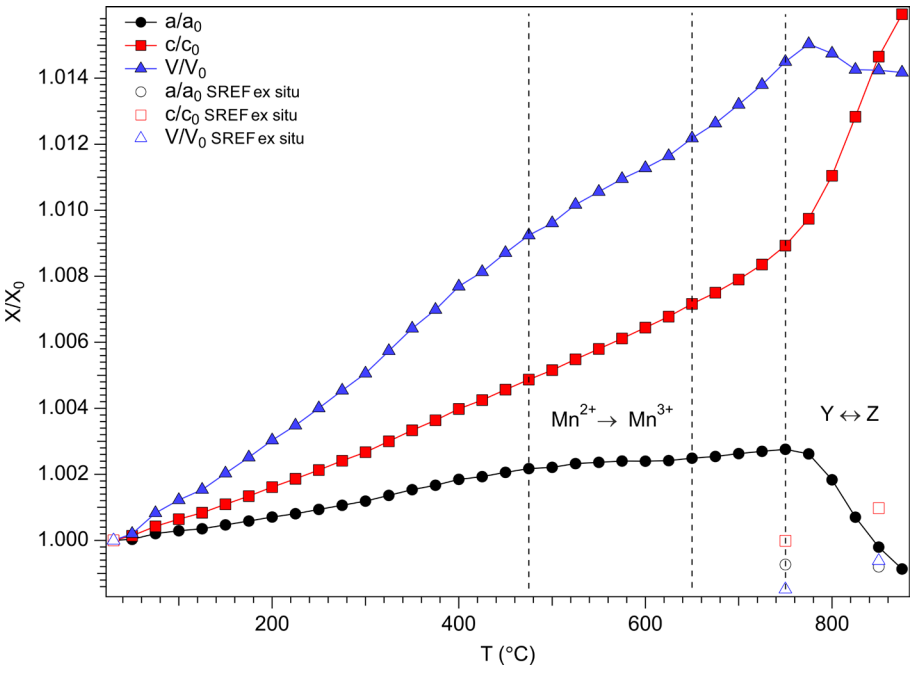

Fig. 4 Change of normalized unit-cell parameters with T for the tourmaline studied.

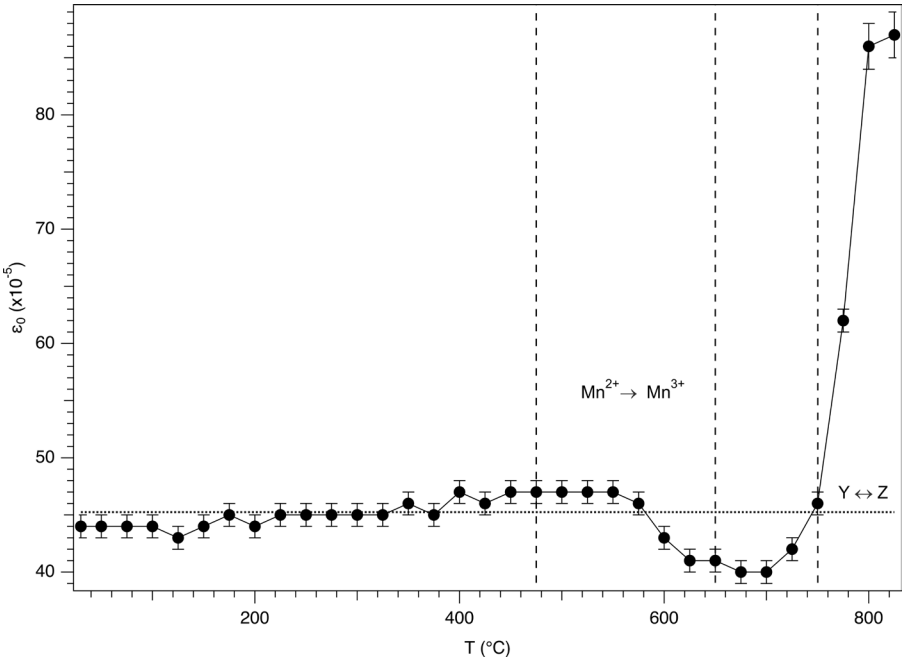

Fig. 5 Variation of ε_0 microstrain with *T* for the tourmaline studied. The dotted horizontal line, corresponding to the ε_0 value at ambient *T*, is drawn as a guide for the eye.

The behavior of the tourmaline unit-cell parameters is quite complex, and several discontinuities were observed. The *a*-parameter deviates from its gradually increasing trend, for the first time, at 500 °C and shows a reduced expansion up to 650 °C, suddenly followed by a restored expansion up to 750 °C; above this *T*, the *a*-parameter contracts significantly, a behavior not observed by Celata et al. (2021) in Fe-rich fluor-elbaite. The *c*-parameter has a more regular behavior; it shows a linear increase until 750 °C; then it is followed by a faster (exponential) expansion rate.

In the case of Fe-rich fluor-elbaite, the deviation of the *a*-parameter from the increasing trend occurs approximately at the same *T,* but it is much more relevant in magnitude. This different behavior can be explained based on the interpretation that has been attributed to this contraction. In the case of Fe-rich fluor-elbaite, the relatively strong shortening of the *a*-parameter has been attributed to the onset of the Fe^{2+} oxidation to Fe^{3+}, counterbalanced by the deprotonation of $(OH)^-$ groups (Celata et al. 2021). Due to the large amount of Fe^{2+} in the pristine fluor-elbaite (0.94 *apfu*), such a process significantly affects the *a*-parameter. On the other hand, in the case of the present tourmaline sample, the relatively small deviation of the *a*-parameter from the increasing trend may be assigned to the onset of the Mn^{2+} oxidation to Mn^{3+}, counterbalanced by the deprotonation of $(OH)^-$ groups. However, the small amount of Mn^{2+} in the pristine tourmaline sample (0.12 *apfu*) produces only minor, albeit detectable, variation in the *a*-parameter.

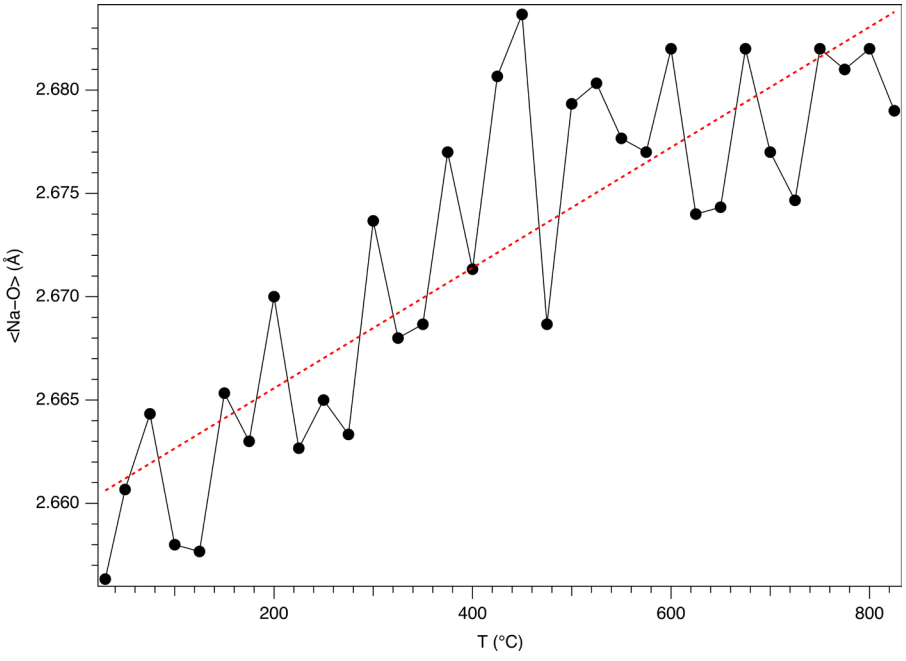

Fig. 6 Variation of <*X*–O> bond distances with *T* for the tourmaline studied.

Analysis of the variation with *T* of the ε_0 microstrain (lattice strain), which is defined as $\beta_i = 4\varepsilon_0 \tan\theta$ (β_i = integral breadth of the j^{th} reflection), optimized during the Rietveld refinements (Ballirano and Sadun 2009), reveals differences with respect to fluor-elbaite. Whereas in the

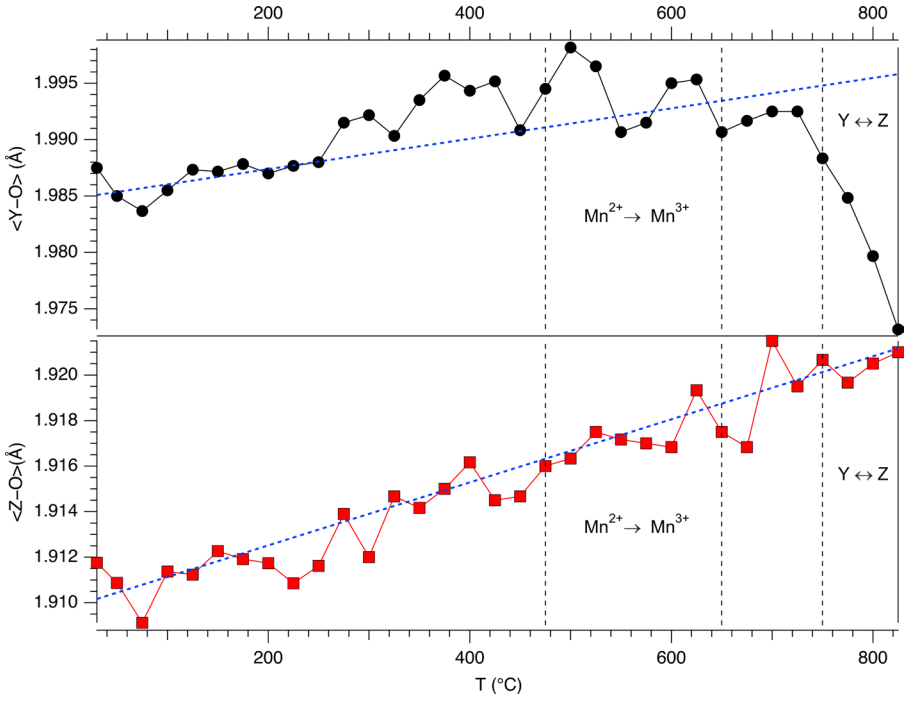

Fig. 7 Dependence of <*Y*–O> (upper panel) and <*Z*–O> (lower panel) bond distances from *T* for the tourmaline studied.

case of fluor-elbaite ε_0 shows a significant increase in the same thermal range where the unit-cell parameters deviate from the regular trends. The present tourmaline sample experiences a minor reduction at *T* slightly higher than those at which Mn oxidation occurs. Subsequently, in correspondence with the abrupt *a*-parameter contraction, ε_0 markedly increases (Fig. 5). Differences in the magnitude of the transient variations of ε_0 are related to the different amounts of oxidized transition elements (and corresponding deprotonation) in the two samples.

Analysis of the structural changes reveals that the <*X*–O> mean bond distance shows a fairly regular increase with *T* (Fig. 6). The dependence of <*Y*–O> and <*Z*–O> bond distances on *T* highlights their different behavior (Fig. 7). In particular, <*Z*–O> regularly increases up to the breakdown, whereas <*Y*–O> marginally increases up to 750 °C, and then contracts up to the breakdown *T*. The interpretation of the observed <*Y*–O> contraction at the same *T* at which the *a*-parameter exhibits a significant contraction is not easy (this point is discussed below).

3.2.3. Compression of the structure near the breakdown temperature: Al-Li disorder

Figure 8 shows the variation of the site scattering (s.s) at the *Y* and *Z* sites with temperature. As can be seen and expected, s.s. are reasonably constant up to 750 °C; their mean values are: *Y* = 31.29(15) electrons per formula unit (*epfu*) and *Z* = 76.86(18) *epfu*. Near breakdown temperature, the start of the migration of s.s. from *Z* to *Y* site indicates an onset of an intracrystalline cation ex-

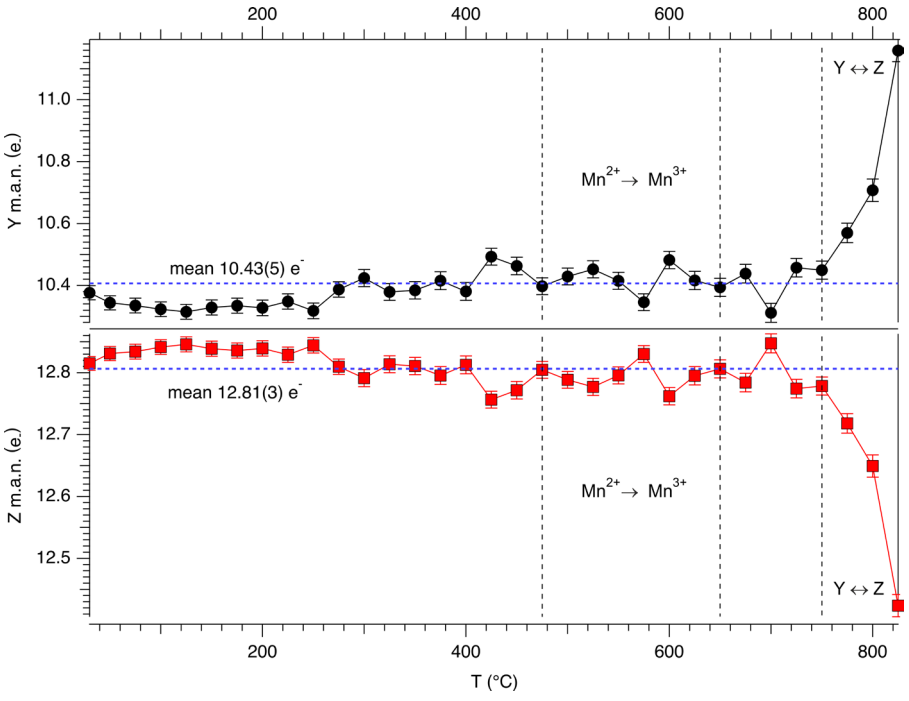

Fig. 8 Evolution with *T* of the site scattering (in *epfu*) at the *Y* (upper panel) and *Z* (lower panel) sites for the tourmaline studied.

change process. The unique process that we can invoke is that some amounts of Li migrate from the slightly larger YO_6 polyhedron to the adjacent slightly smaller $^{Z}AlO_6$ polyhedron, which makes Al move to the *Y* site. Because the empirical ionic radii of $^{[6]}$Li and $^{[6]}$Al are 0.751(9) and 0.547(3) Å, respectively (Bosi 2018), the small contraction of <*Y*–O> may be explained by the intracrystalline order-disorder reaction $^{Y}Li + {}^{Z}Al \rightarrow {}^{Z}Li + {}^{Y}Al$, which has not been documented so far. The expected increased expansion of <*Z*–O> might be possibly masked by thermal expansion effects and by the double multiplicity of the *Z* site with respect to *Y*. From refined s.s., ca. 0.09 Li pfu are expected to be exchanged at 825 °C. This value is in line with that inferred from SC-XRD (see above) and possibly extends to ca. 0.18 *apfu* at 870 °C, but this result should be accepted with caution owing to potential correlations caused by the occurrence in a mixture of both mullite-like phase and γ-$LiAlSi_2O_6$. It is worth noting that in the case of the present tourmaline sample, the difference between <*Y*–O> and <*Z*–O> in the whole explored thermal range (0.05–0.08 Å) is significantly smaller than that of Fe-rich fluor-elbaite (0.08–0.13 Å), perhaps facilitating the onset of the proposed order-disorder reaction.

Moreover, the different thermal behavior with respect to Fe-rich fluor-elbaite is also given in terms of different crystalline breakdown products, in particular γ-$LiAlSi_2O_6$.

4. Conclusions

A purplish-red Mn-bearing elbaite was structurally investigated through both *in situ* and *ex situ* H*T* experiments with the results of which ended up being in a fairly reasonable agreement. At above 470 °C, a shrink of the unit-cell *a*-parameter was observed along with the downsizing of the YO_6 polyhedron, owing to the thermally induced oxidation of Mn^{2+} into Mn^{3+}. A further contraction of the *a*-parameter and <*Y*–O> above 752 °C was explained as a partial Li-Al disorder between the *Y* and *Z* sites.

The breakdown temperature of Mn-bearing elbaite was constrained at 825 °C with the detection of the first breakdown product represented by B-mullite. The breakdown products from the HT-pXRD experiments were collected and identified at ambient temperature via pXRD, being mostly represented by B-mullite and γ-$LiAlSi_2O_6$.

Acknowledgments: Sapienza University of Rome grant (Prog. Università 2020 to F. Bosi) is gratefully acknowledged.

Electronic supplementary material. The crystallographic information file (CIF) for both of described structures are available online at the Journal web site (*http://dx.doi.org/10.3190/jgeosci.347*).

References

Bačík P, Ozdín D, Miglierini M, Kardošová P, Pentrák M, Haloda J (2011) Crystallochemical effects of heat treatment on Fe-dominant tourmalines from Dolnı´ Bory (Czech Republic) and Vlachovo (Slovakia). Phys Chem Miner 38: 599–611

Ballirano P (2003) Effects of the choice of different ionization level for scattering curves and correction for small preferred orientation in Rietveld refinement: the $MgAl_2O_4$ test case. J Appl Crystallogr 36: 1056–1061

Ballirano P, Maras A (2006) In-situ X-ray transmission powder diffraction study of the kinetics of the light induced alteration of realgar (α-As_4S_4). Eur J Mineral 18: 589–599

Ballirano P, Melis E (2007) Thermal behaviour of β-anhydrite $CaSO_4$ to 1,263K. Phys Chem Miner 34: 699–704

Ballirano P, Sadun C (2009) Thermal behavior of trehalose dihydrate (T_h) and β-anhydrous trehalose (T_β) by in-situ laboratory parallel-beam X-ray powder diffraction. Struct Chem 20: 815–823

Bosi F (2018) Tourmaline crystal chemistry. Amer Miner 103: 298–306

Bosi F, Skogby H, Hålenius U (2019) Thermally induced cation redistribution in fluor-elbaite and Fe-bearing tourmalines. Phys Chem Miner 46: 371–383

Bosi F, Celata B, Skogby H, Hålenius U, Tempesta G, Ciriotti ME, Bittarello E, Marengo A (2021) Mn-bearing purplish-red tourmaline from the Anjanabonoina pegmatite, Madagascar. Mineral Mag 85: 242–253

Buick I, Grew ES, Armbruster T, Medenbach O, Yates MG, Bebout, GE, Clarke GL (2008) Boromullite, $Al_9B-Si_2O_{19}$, a new mineral from granulite-facies metapelites, Mount Stafford, central Australia and a natural analogue of a synthetic "boron-mullite". Eur J Mineral 20: 935–950

Bruker AXS (2016) Topas V6: General profile and structure analysis software for powder diffraction data. Bruker AXS, Karlsruhe, Germany.

Castañeda C, Eeckhout SG, da Costa GM, Botelho NF, De Grave E (2006) Effect of heat treatment on tourmaline from Brazil. Phys Chem Miner 33: 207–216

Celata B, Ballirano P, Andreozzi GB, Bosi F (2021) In-situ high-temperature behaviour of fluor-elbaite: breakdown conditions and products. Phys Chem Miner 48: 24

Cempírek J, Grew ES, Kampf AR, Ma C, Novák M, Gadas P, Škoda R, Vašinová-Galiová M, Pezzotta F, Groat LA, Krivovicev SV (2016) Vránaite, ideally $Al_{16}B_4Si_4O_{38}$, a new mineral related to boralsilite, $Al_{16}B-_6Si_2O_{37}$, from the Manjaka pegmatite, Sahatany Valley, Madagascar. Amer Miner 101: 2108–2117

Cheary RW, Coelho AA (1992) A Fundamental Parameters Approach of X-ray line-profile fitting. J Appl Crystallogr 25: 109–121

Dutrow BL, Henry D (2011) Tourmaline: A geologic DVD. Elements 7(5): 301–306

French BM, Jezek PA, Appleman DE (1978) Virgilite: a new lithium aluminum silicate mineral from the Macusani glass, Peru. Amer Miner 63: 461–465

Fuchs Y, Lagache M, Linares J, Maury R, Varret F (1995) Mössbauer and optical spectrometry of selected schörl–dravite tourmalines. Hyperfine Interact 96: 245–258.

Fuchs Y, Lagache M, Linares J (2002) Oxydation expérimentale de Fe-tourmalines et corrélation avec une déprotonation des groupes hydroxyle. C R Geosci 334: 245–249

Grew ES, Graetsch HA, Pöter B, Yates MG, Buick I, Bernhardt H-J, Schreyer W, Werding G, Carson CJ, Clarke GL (2008) Boralsilite, $Al_{16}B_6Si_2O_{37}$, and "boron-mullite:" Compositional variations and associated phases in experiment and nature. Amer Miner 93: 283–299

Henry DJ, Novák M, Hawthorne FC, Ertl A, Dutrow BL, Uher P, Pezzotta F (2011) Nomenclature of the tourmaline-supergroup minerals. Amer Miner 96: 895–913

Li C-T (1968) The crystal structure of $LiAlSi_2O_6$ III (high-quartz solid solution). Z Kristallogr 127: 327–348

Lührs H, Soellradl S, King SP, Hanna JV, Konzett J, Fischer RX (2014) Ambient and high-pressure synthesis, composition, and crystal structure of B-mullites. Cryst Res Technol 49: 21–31

Novák M, Cempírek J, Gadas P, Škoda R, Vašinová-Galiová M, Pezzotta F, Groat LA (2015) Boralsilite and Li,Be-bearing "boron mullite" $Al_8B_2Si_2O_{19}$, breakdown products of spodumene from the Manjaka pegmatite, Sahatany Valley, Madagascar. Canad Mineral 53: 357–374

Ota T, Kobayashi K, Kunihiro T, Nakamura E (2008) Boron cycling by subducted lithosphere; insights from diamondiferous tourmaline from the Kokchetav ultra-high-pressure metamorphic belt. Geochim Cosmochim Acta 72: 3531–3541

Pieczka A, Kraczka J (2004) Oxidized tourmalines – a combined chemical, XRD and Mössbauer study. Eur J Mineral 16: 309–321

Sabine TM, Hunter BA, Sabine WR, Ball CJ (1998) Analytical expressions for the transmission factor and peak shift in absorbing cylindrical specimens. J Appl Crystallogr 31: 47–51

Sheldrick GM (2015) Crystal structure refinement with SHELXL. Acta Crystallogr C71: 3–8

van Hinsberg V, Henry DJ, Marschall HR (2011) Tourmaline: an ideal indicator of its host environment. Canad Mineral 49: 1–16

Werding G, Schreyer W (1992) Synthesis and stability of werdingite, a new phase in the system $MgO–Al_2O_3–B_2O_3–SiO_2$ (MABS), and another new phase in the ABS-system. Eur J Mineral 4: 193–207

Young R (1993) Introduction to the Rietveld method. In: Young RA (ed) The Rietveld method. Oxford University Press, pp 1–38